

On the compact HII galaxy UM 408 as seen by GMOS-IFU: Physical conditions.

Patricio Lagos^{1,2}

plagos@iac.es

Eduardo Telles^{1,3}

etelles@on.br

Casiana Muñoz-Tuñón²

cmt@iac.es

Eleazar R. Carrasco⁴

rcarrasco@gemini.edu

François Cuisinier⁵

francois@ov.ufrj.br

and

Guillermo Tenorio-Tagle⁶

gtt@inaoep.mx

ABSTRACT

¹Observatório Nacional, Rua José Cristino, 77, Rio de Janeiro, 20921-400, Brazil

²Instituto de Astrofísica de Canarias, Via Láctea s/n, 38200 La Laguna, Spain

³Dept. of Astronomy, University of Virginia, P.O.BOX 400325, Charlottesville, VA, 22904-4325, USA

⁴Gemini Observatory/AURA, Southern Operations Center, Casilla 603, La Serena, Chile

⁵Observatório do Valongo UFRJ, Ladeira do Pedro Antônio 43, Rio de Janeiro, 20080-090, Brazil

⁶Instituto Nacional de Astrofísica Óptica y Electrónica, AP 51, 72000 Puebla, México

We present Integral Field Unit GMOS-IFU data of the compact HII galaxy UM 408, obtained at Gemini South telescope, in order to derive the spatial distribution of emission lines and line ratios, kinematics, plasma parameters, and oxygen abundances as well the integrated properties over an area of $3'' \times 4''.4$ equivalent with $\sim 750 \times 1100$ pc located in the central part of the galaxy. The starburst in this area is resolved into two giant regions of about $1''.5$ and $1''$ (~ 375 and ~ 250 pc) diameter, respectively and separated 1.5 - $2''$ (~ 500 pc). The extinction distribution concentrate its highest values close but not coincident with the maxima of $H\alpha$ emission around each one of the detected regions. This indicates that the dust has been displaced from the exciting clusters by the action of their stellar winds. The ages of these two regions, estimated using $H\beta$ equivalent widths, suggest that they are coeval events of ~ 5 Myr with stellar masses of $\sim 10^4 M_{\odot}$. We have also used $[OIII]/H\beta$ and $[SII]/H\alpha$ ratio maps to explore the excitation mechanisms in this galaxy. Comparing the data points with theoretical diagnostic models, we found that all of them are consistent with excitation by photoionization by massive stars. The $H\alpha$ emission line was used to measure the radial velocity and velocity dispersion. The heliocentric radial velocity shows an apparent systemic motion where the east part of the galaxy is blueshifted, while the west part is redshifted, with a relative motion of ~ 10 km s $^{-1}$. The velocity dispersion map shows supersonic values typical for extragalactic HII regions. Oxygen abundances were calculated from the $[OIII]\lambda\lambda 4959,5007/[OIII]\lambda 4363$ ratios. We derived an integrated oxygen abundance of $12+\log(O/H)=7.87$ summing over all spaxels in our field of view. An average value of $12+\log(O/H)=7.77$ and a difference of $\Delta(O/H)=0.47$ between the minimum and maximum values (7.58 ± 0.06 - 8.05 ± 0.04) were found, considering all data points where the oxygen abundance was measured. The spatial distribution of oxygen abundance does not show any significant gradient across the galaxy. On the other hand, the bulk of data points are lying in a region of $\pm 2\sigma$ dispersion (with $\sigma=0.1$ dex) around the average value, confirming that this compact HII galaxy as other previously studied dwarf irregular galaxies is chemically homogeneous. Therefore, the new metals processed and injected by the current star formation episode are possibly not observed and reside in the hot gas phase, whereas the metals from previous events are well mixed and homogeneously distributed through the whole extent of the galaxy.

Subject headings: galaxies: individual (UM 408) — galaxies: abundances — galaxies: dwarf — galaxies: ISM.

1. Introduction

HII galaxies (or Blue Compact Dwarfs, BCDs) are low-mass and metal-poor galaxies ($1/50$ - $1/3Z_{\odot}$), experiencing strong episodes of star formation, characterized by the presence of bright emission lines on a faint blue continuum (Terlevich et al. 1991; Kehrig et al. 2004). Several studies (e.g, Papaderos et al. 1996; Telles & Terlevich 1997; Cairós et al. 2003; Westera et al. 2004) have shown the existence of an old stellar population underlying the present burst in most of these galaxies, indicating that these objects are not young systems forming their first generation of stars.

The star formation activity in HII galaxies is concentrated in several luminous star clusters (~ 1 - 30 pc in size) spread over the galaxies. Some of these clusters have been associated with super star clusters (SSCs), similar to those found in interacting galaxies, such as the antennae (Whitmore & Schweizer 1995; Whitmore et al. 1999), and some local dwarf galaxies such as Henize 2-10 (Conti & Vacca 1994) and NGC 1569 (e.g., O’Connell et al. 1994; Arp & Sandage 1985). During their evolution, these clusters ionize the interstellar medium (ISM) causing the formation of giant HII regions (GHIIRs), and release a considerable quantity of mechanical energy into the ISM, characterized by supersonic motions (e.g, Melnick et al. 1987), sweeping up the surrounding medium, removing the gas and dust from the star formation site, while producing structures such as bubbles and supershells. Ultimately, the evolution of these young clusters also causes the freshly produced metals to be dumped into the ISM.

Oxygen and other α elements are produced by massive stars (>8 - $10 M_{\odot}$) and are released into the ISM during their supernova phase. These metals will be dispersed in the whole galaxy and mixed via hydrodynamic mechanisms in time scales of few 10^8 yrs (e.g., Tenorio-Tagle 1996). Since the spatial distribution of abundances of O, N, etc depends on the recycling time of the ISM, the spatial variation of these abundances give important insights about these processes. The spatial distribution of emission line ratios and of the abundance of certain elements in dwarf galaxies have been studied by different authors (e.g., Kobulnicky & Skillman 1996, 1997; Lee et al. 2006). In these works the radial and spatial distribution of the O/H abundance, obtained from the analysis of their H II regions, have been used as a chemical evolution indicator. Localized nitrogen self enrichment has been measured in a few cases and attributed to the action of strong winds produced by Wolf-Rayet (W-R) stars (e.g., Walsh & Roy 1989; Kobulnicky et al. 1997), but no oxygen localized enrichment systems have been confirmed (Kobulnicky & Skillman 1996). In GHIIRs, where only one star formation region is present, it is usually assumed that the abundance of the galaxy and their ISM is well represented by the abundance of this single region, assuming that the metals are well mixed and distributed across the galaxy.

The details of the structure of HII galaxies are important to understand their ionization mechanisms, star formation feedback and chemical enrichment. These issues have been actively addressed in studies of the brightest and nearest systems. The large and heterogeneous HII galaxy sample (Loose & Thuan 1986; Kunth et al. 1988; Telles et al. 1997) includes a significant number of far less studied objects at larger distances, with small apparent sizes and with relatively low surface brightness. Typically, HII galaxies contain one or a few star formation regions, but $H\beta$ images (Lagos et al. 2007) of some compact objects have revealed that the central region probably hosts a myriad of unresolved star clusters. The present facilities, with high spatial resolution and high efficiency instruments on large telescopes (8m), allow us to study these more distant objects to derive their observed properties and relate them to the better known nearby galaxies, thus having a handle on the intrinsic properties of star formation as well as possible evolutionary effects.

In this paper we use integral field spectroscopy with Gemini Multi-object Spectrograph and the Integral Field Unit (GMOS-IFU) at Gemini South in order to study the spatial distribution of emission lines, their ratios, extinction, abundances and the kinematic properties of the gas in the interstellar medium of the compact dwarf galaxy UM 408. UM 408 belongs to a subset sample of rare HII galaxies with low metal abundances (i.e. $Z < 1/20 Z_{\odot}$) with $12 + \log(O/H) = 7.66$ (Masegosa et al. 1994; Telles 1995), compact morphology, and very small effective radius (R_{eff}) of only $2''.1$ from previous morphology and surface brightness studies (Telles & Terlevich 1997). On other hand, Pustilnik et al. (2002) using high resolution spectroscopy derived an abundance of $12 + \log(O/H) = 7.93$ and HI observations (Salzer et al. 2002) reveal an HI mass of $\log(M_{HI}) = 8.815 M_{\odot}$. UM 408 is cataloged by Salzer (1989) as a Dwarf HII Hot Spot with a redshift of 0.012^1 ($v = 3598 \text{ km s}^{-1}$) with coordinates $RA = 02^h 11^m 23^s.4$, $DEC = 02^{\circ} 20' 30''$ (J2000) at a distance of $\sim 46 \text{ Mpc}$, and V apparent magnitude of 17.38. With the present observations, we note that the central part of UM 408 encompasses two main star formation regions (here named A and B), as shown by the g-band acquisition images in Figure 1. Another faint region, called C, can be seen in the outer parts of the galaxy. These regions were all unresolved in previous studies.

The observations and data reduction procedures are discussed in Section 2. Section 3 gives the results obtained from the 2D emission line maps. In Section 4 we discuss our results and our conclusions are presented in section 5.

¹Value obtained from NED

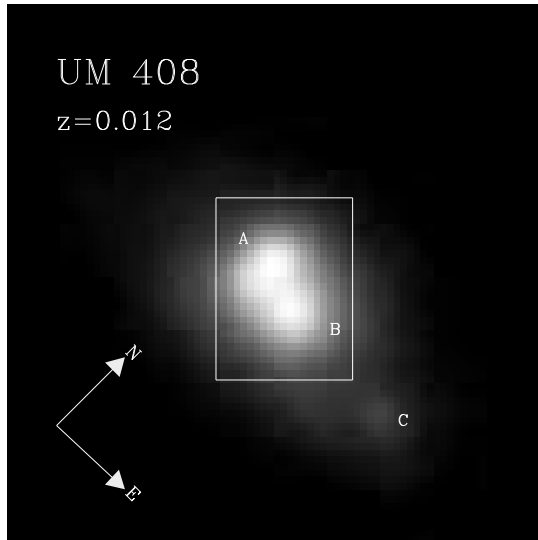


Fig. 1.— g-band acquisition image of the galaxy UM 408. The image is $11''.5 \times 11''.5$. The rectangle indicates the field of view of $3'' \times 4''.4$ ($\sim 750 \times 1100$ pc) used in this work to construct the monochromatic maps. The two most prominent regions (A and B) are indicated in the image. The faint region (C in the plot) located $\sim 3''.0$ to the East from B is placed outside the field of view ($1'' \simeq 250$ pc).

2. Observations and Data Reductions

The observations were performed with the Gemini Multi-Object Spectrograph GMOS (Hook et al. 2004) and the IFU unit (Allington-Smith et al. 2002, hereafter GMOS-IFU) at Gemini South Telescope in Chile during the night of August 21 and December 31 2004, using the grating B600+_G5323 (B600) and on January 01, 2005 with the grating R600+_G5324 (R600) in one slit mode, covering a total spectral range from ~ 3021 to 7225 \AA . The GMOS-IFU in one slit mode composes a pattern of 750 hexagonal elements, each with a projected diameter of $0''.2$, covering a total $3''.5 \times 5''$ field of view, where 250 of these elements are dedicated to sky observation. The detector is formed by three 2048×4608 CCDs with $13.5 \mu\text{m}$ pixels, with a scale of $0.073''/\text{pixel}$. The CCDs create a mosaic of 6144×4608 pixels with a small gap between the chips of 37 columns.

Table 1 shows the observing log, indicating the instrumental setup, airmass and exposure

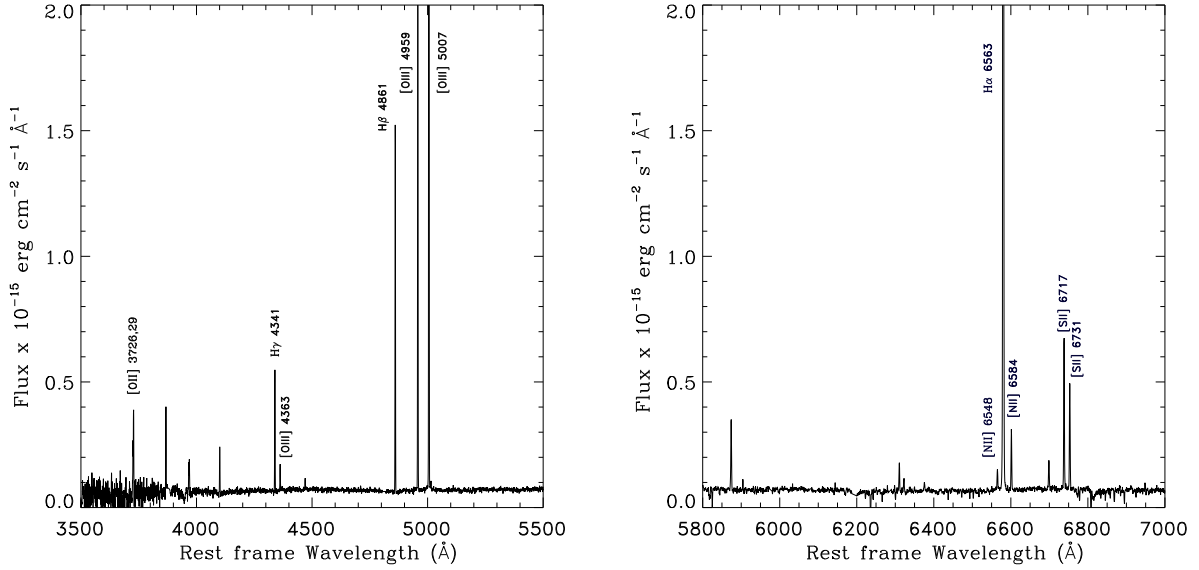


Fig. 2.— 1D blue and red parts of the spectrum, obtained as the sum of all fibers, in the rest-frame wavelength. In this Figure, only the lines used in the analysis are indicated.

times, the dispersion, the final resolution and the seeing (FWHM) of each observation. The data were reduced using the Gemini package version 1.8 inside IRAF². All science exposures, comparison lamps and spectroscopic twilight and GCAL flats were overscan/bias subtracted and trimmed. The spectroscopic GCAL flats were processed by removing the calibration unit plus GMOS spectral response and the calibration unit uneven illumination. Twilight flats were used to correct for the illumination pattern in the GCAL lamp flat using the task `gfresponse` in the GMOS package. The twilight spectra were divided by the response map obtained from the lamp flats and the resulting spectra were averaged in the dispersion direction, giving the ratio of sky to lamp response for each fiber. The final response maps were obtained then by multiplying the GCAL lamp flat by the derived ratio. The resulting extracted spectra were then wavelength calibrated, corrected by the relative fiber throughputs, and extracted. The residual values in the wavelength solution for 60-70 points using a 4th or 5th Chebyshev polynomial typically yielded *rms* values of ~ 0.10 Å and ~ 0.15 Å for both gratings respectively. The final spectra cover a wavelength interval of ~ 3021 – 5823 Å and ~ 4371 – 7225 Å for data taken with the B600 and R600 gratings, respectively. The final spectral resolutions and dispersions are shown in Table 1 (columns 5

²IRAF is distributed by NOAO, which is operated by the Association of Universities for Research in Astronomy Inc., under cooperative agreement with the National Science Foundation.

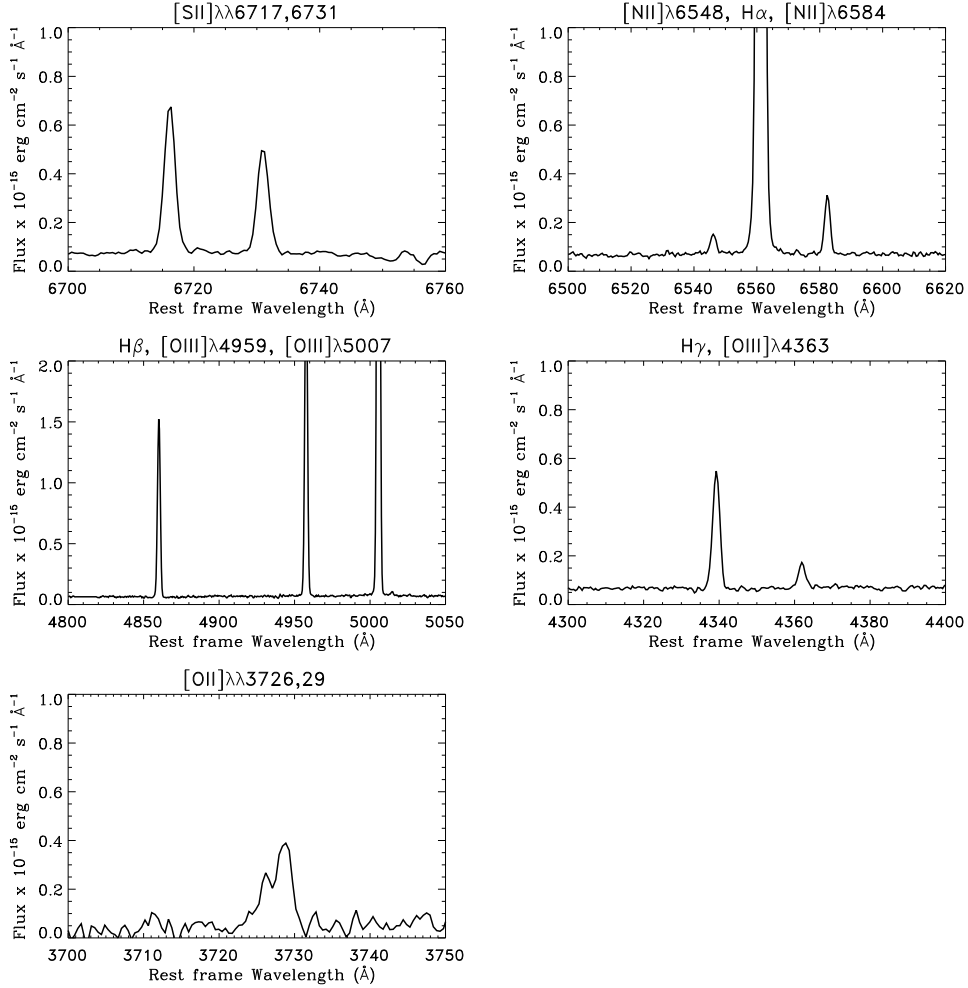


Fig. 3.— Subsets from the spectra in Figure 2 showing details of selected emission lines considered in this study.

and 6).

The flux calibration was performed using the sensitive function derived from observation of the star LTT 3864 for both gratings in December 31 and January 1. Standard stars were not observed in August. Therefore, the blue part of the spectra was constructed using only the observation obtained in December 2004. The 2D data images were transformed into 3D data cube (x,y,λ) using the *gfcube* routine and resampled as square pixels with 0^{''}.1 of spatial resolution. The emission line fluxes were measured using the IRAF task *fitprofs* by fitting Gaussian profiles. From these, we then created the emission line maps used in our analysis (see Section 3).

At shorter wavelength the IFU spectroscopy and long-slit observations suffer a spatial translation produced by differential atmospheric refraction (DAR). This effect is wavelength dependent, and is produced by the deviation of the light when it passes through the atmosphere due to the variation of the air density as a function of elevation. In order to obtain fluxes corrected of DAR, we used a similar procedure as described in Arribas et al. (1999) and also applied by Westmoquette et al. (2007a). First we splitted the data cube in monochromatic images, and for each image we calculated the centroid of an unresolved point source in the field of view, that in our case corresponds to region A. Finally, the various monochromatic maps were aligned by shifting the centroids to the same position.

In Figure 2 we show the resultant spectrum for the two gratings used, obtained from the sum of all GMOS-IFU fibers. Figure 3 shows a detailed view of the selected emission lines considered in this study. The spectral resolution of the GMOS-IFU observations allow us to resolve the [OII] $\lambda\lambda$ 3726,29 doublet lines in a limited number of apertures with a $\Delta\lambda=2.32 \text{ \AA}$ between the peak of the lines in the integrated spectrum (see Figure 3). The low intensity of [OII] $\lambda\lambda$ 3726,29 lines and [OIII] λ 4363 are the largest sources of uncertainties in our results. An automatic procedure to measure these emission line fluxes was not possible, therefore these lines were measured manually using *plot*.

3. Results

3.1. Emission line, continuum and EW(H β) maps

We used a flux measurement procedure described in the previous section to produce the maps for the following emission lines: [SII] λ 6731, [SII] λ 6717, [NII] λ 6584, H α , [OIII] λ 5007, [OIII] λ 4959, H β , [OIII] λ 4363, H γ , [OII] $\lambda\lambda$ 3726,29, H α and H β continuum and EW(H β), in a rectangular field of $3'' \times 4''.4$ (see Figure 1). In order to reduce the number of data points without losing spatial information and S/N, the data were resampled to $0''.2$ in spatial resolution. Typical S/N ratios for individual pixels (spaxels in our data cube) for [OIII] λ 5007 are $\gtrsim 700$ and $\gtrsim 500$ for regions A and B, respectively. The [OIII] λ 4363 line shows a typical S/N ratio $\gtrsim 8$ and $\gtrsim 4$ for regions A and B, respectively. The signal to noise for each emission line is given by the ratio between the emission line peak and the RMS of the adjacent continuum. Figure 4 shows some of the observed emission line maps. All emission and continuum maps in this Figure are in units of $\times 10^{-18} \text{ erg cm}^{-2} \text{ s}^{-1}$, except for the H β equivalent width map, which is in units of \AA . Here $0''.2 \approx 50 \text{ pc}$ (distances in this work were computed assuming a Hubble constant of $H_0=72 \text{ km s}^{-1} \text{ Mpc}^{-1}$). Since most of the emission lines were measured using an automatic procedure, we filtered the maps assigning the value $0 \text{ erg cm}^{-2} \text{ s}^{-1}$ to all pixels with $S/N < 3$.

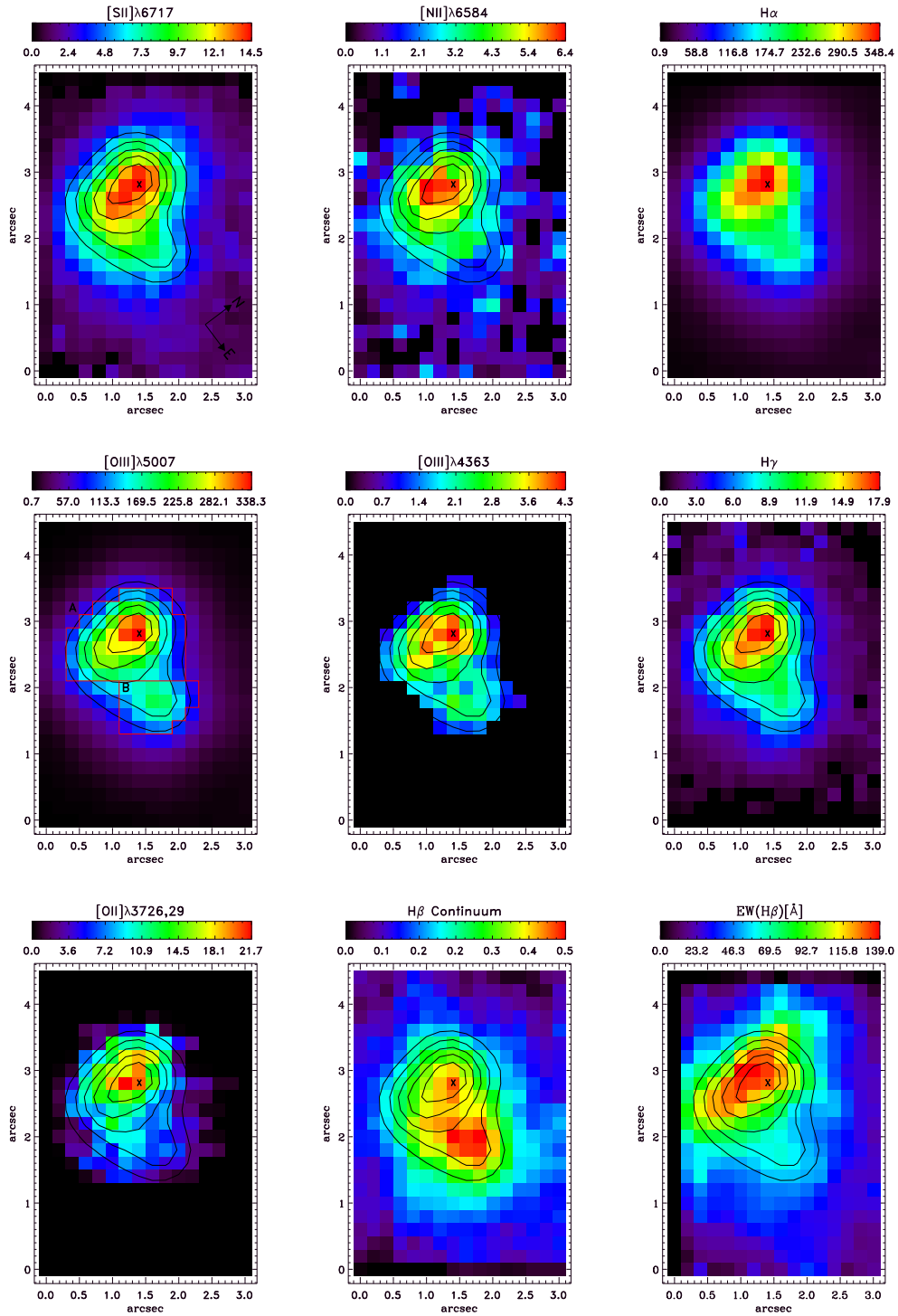


Fig. 4.— Observed maps for [SII] λ 6717, [NII] λ 6584, H α , [OIII] λ 5007, [OIII] λ 4363, H γ and [OII] λ 3726,29 emission lines, H β continuum and EW(H β). Fluxes in units of $\times 10^{-18}$ erg cm $^{-2}$ s $^{-1}$ and EW(H β) in units of \AA . H α emission line contours are overplotted on all maps. The maximum H α emission is placed over region A and is indicated in the maps by an X symbol. The regions in the [OIII] λ 5007 map mark the areas considered as regions A and B.

The maps in Figure 4 show essentially the same spatial distribution, presenting two well defined and regular regions, that we have labeled A and B. The maximum peak intensity of the H α emission line in region A is indicated in the maps by an X symbol. The recombination lines H α , H β and H γ have very similar spatial distribution to the forbidden lines in Figure 4, but there is a slight difference in the spatial distribution of [OIII] λ 4363 and [OII] λ λ 3726,29 over region B. The last two images in Figure 4 corresponds to the spatial distribution of the H β continuum and the EW(H β), respectively. It is clear from the maps that the continuum peak is not coincident with the maximum in H α emission. This has been previously reported by other authors (e.g., Sargent & Filippenko 1991; Maiz-Apellaniz et al. 1998; Lagos et al. 2007) in some galaxies with single and multiple star forming regions. In NGC 4214, Sargent & Filippenko (1991) and Maiz-Apellaniz et al. (1998) found that the continuum peak emission was displaced in relation to the line emitting regions where a strong Wolf-Rayet (WR) feature (HeII λ 4686 Å) was also seen. No WR signatures were detected in the spectra of UM 408.

The largest EW(H β) values in the galaxy are associated with region A, indicating that this region is younger than region B. On the other hand, the H β continuum map (see Figure 4) shows the largest values over region B. In Section 4, the EW(H β) values are used as a proxy for the starburst ages in order to derive the integrated physical properties of the galaxy and their star forming regions. The error associated to each emission line (σ_i) was calculated using the relationship given in Castellanos et al. (2002):

$$\sigma_i = \sigma_c N^{1/2} \sqrt{1 + \frac{EW}{N\Delta}}, \quad (1)$$

where σ_c is the standard deviation in the local continuum associated to each emission line, N is the number of pixels, EW is the equivalent width of the line and Δ is the instrumental dispersion in Å (see Table 1). These estimated errors will be used later in the derivation of uncertainties in the oxygen abundance determination and integrated properties.

Finally, given that the seeing was 0.8-0.9'' (\sim 4 pixels in the emission line maps), each aperture or pixel of 0.2'' should be correlated with its neighbor, and the pixel-to-pixel variations in the maps produced from the observed emission line are likely due to the uncertainties attached to the measurement and do not represent real variations. Therefore, we smoothed the emission line ratio, temperature and oxygen abundance maps using a 3 \times 3 box.

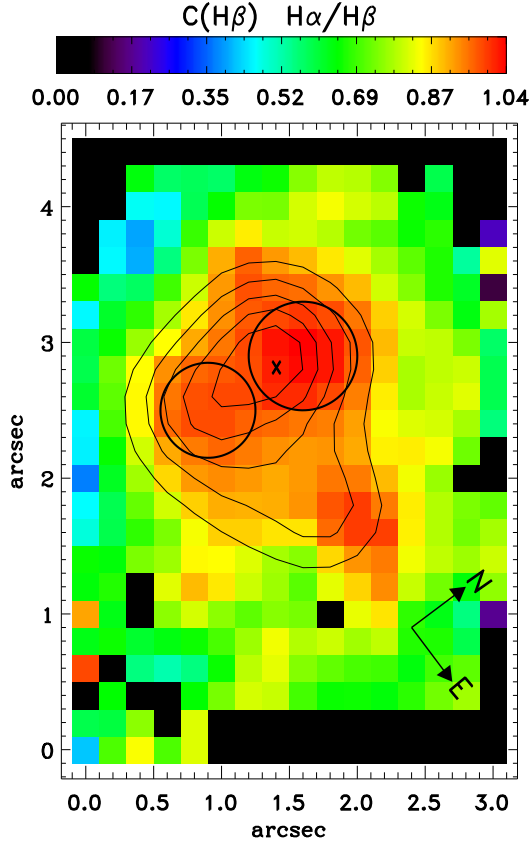


Fig. 5.— Extinction coefficient distribution, obtained from the emission lines $H\alpha/H\beta$ ratios. The regions enclosed by circles mark the location of other extinction peaks, probably related to other unresolved star clusters. The maximum $H\alpha$ emission is placed over region A and is indicated by an X symbol. $H\alpha$ contours are overplotted on the maps.

3.2. Extinction

The logarithmic reddening parameter $c(H\beta)$ was calculated from the ratio $H\alpha/H\beta$, where the intrinsic value of 2.87 for case B recombination was assumed. Thus, the corrected emission lines are calculated as

$$\frac{I(\lambda)}{I(H\beta)} = \frac{F(\lambda)}{F(H\beta)} \times 10^{c(H\beta)f(\lambda)}, \quad (2)$$

where $I(\lambda)$ and $F(\lambda)$ are the dereddened flux and observed flux at a given wavelength, respectively and $f(\lambda)$ is the reddening function given by Seaton (1979) as parametrized by

Howarth (1983), using appropriated values for the Milky Way (Kobulnicky et al. 1997).

Figure 5 shows the smoothed spatial distribution of $c(H\beta)$ for the emission line ratios mentioned above. The reddening parameters $c(H\beta)$ were set to 0.0 for unrealistic values of $H\alpha/H\beta < 2.87$. We observe a range of extinction of ~ 0.02 to 1.04 with average $c(H\beta)$ value of 0.76 and a standard deviation of 0.17. The lowest extinction values are located in the outer part of the field of view (see Figure 5). We note also that the maximum extinction $c(H\beta)$ is close to, but not coincident with the peak of $H\alpha$ emission. A similar result has been reported by Maiz-Apellaniz et al. (1998) and Cairós et al. (2002) for the star formation knots in the galaxies NGC 4214 and Mrk 370, respectively. Apparently, the current starburst episode in this galaxy is sweeping the gas and dust out of the center into the surrounding regions. The emission line distribution as well as the $c(H\beta)$ distribution over region A and its elongated shape suggest that this region may contain two or more star forming complexes instead of only one. These complexes are indicated with circles in the extinction maps.

Finally, as the extinction across the galaxy does not show a uniform distribution, concentrating the highest values around the star forming regions, the fluxes of each pixel in the emission line maps were corrected using their corresponding $c(H\beta)$ value.

3.3. Nebular emission line diagnostic diagrams

The standard BPT diagnostic diagrams (Baldwin et al. 1981) have been used to analyze the possible excitation mechanisms present in UM 408. Figure 6 (a, b and c) shows the following emission line ratio maps: $[OIII]\lambda 5007/H\beta$ ($[OIII]/H\beta$), $[SII]\lambda\lambda 6717,6731/H\alpha$ ($[SII]/H\alpha$) and $[NII]\lambda 6584/H\alpha$ ($[NII]/H\alpha$). Figure 6 shows that $[OIII]/H\beta$ and $[SII]/H\alpha$ ratios have essentially the same spatial distribution with inverse trends. The largest values of $[OIII]/H\beta$ and the lowest values of $[SII]/H\alpha$ are seen in the east part of the galaxy, near region B. The emission line ratios measured within these regions are common to high excitation HII regions with values ranging from $\log([OIII]/H\beta)=0.45$ to 0.80 (all map), 0.65 to 0.76 (region A) and 0.72 to 0.80 (region B), and from $\log([SII]/H\alpha)=-1.21$ to -0.62 (all map), -1.17 to -0.85 (region A) and -1.21 to -1.01 (region B). Additionally, the low ionization ratios $[NII]/H\alpha$ and $[SII]/H\alpha$ increase from the center outwards.

Figure 7 shows the $\log[OIII]/H\beta$ vs. $\log[SII]/H\alpha$ diagnostic diagram, identifying three different regions in UM 408 using the original data points (non-smoothed). Red and green crosses correspond to regions A and B, respectively, and the black crosses correspond to the outer parts of the galaxy. The integrated value that represents the sum over all spaxels in our field of view is given by the blue star symbol. The solid line in Figure 7 divides the

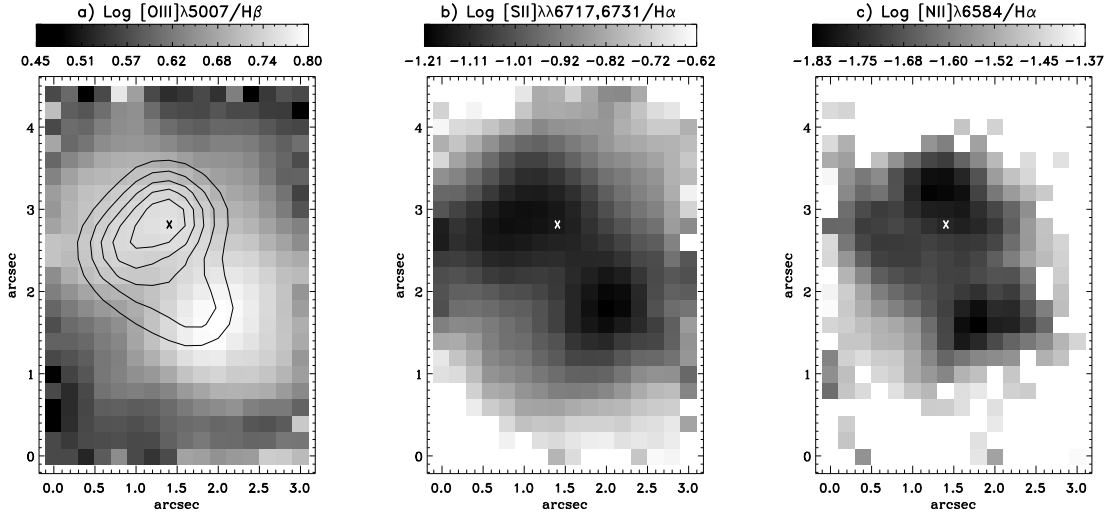


Fig. 6.— Emission line ratios: (a) $\text{Log } [\text{OIII}]\lambda 5007/\text{H}\beta$, (b) $\text{Log } [\text{SII}]\lambda\lambda 6717, 6731/\text{H}\alpha$ and (c) $\text{Log } [\text{NII}]\lambda 6584/\text{H}\alpha$. The maximum $\text{H}\alpha$ emission is placed over region A and is indicated in the maps by an X symbol. $\text{H}\alpha$ contours are overplotted on Figure a).

diagram into two regions that correspond to line ratios explained solely by photoionization by massive stars and to line ratios where an additional source of excitation must be present, as in the case of Active Galactic Nuclei (AGNs; Osterbrock & Ferland 2006). From the distribution of the data in the diagnostic diagram we conclude that the HII regions in UM 408 are produced by photoionization by massive stars.

3.4. Density, temperature and oxygen abundance

The first step in the abundance derivation is to obtain the electron density and temperature. The electron density is obtained using the emission line ratio $[\text{SII}]\lambda 6717/[\text{SII}]\lambda 6731$, and the electron temperature from the ratio $[\text{OIII}]\lambda\lambda 4959, 5007/[\text{OIII}]\lambda 4363$. In Figure 8a we can see that the ratio $[\text{SII}]\lambda\lambda 6717, 6731$ is typically greater than 1 which indicates a low density regime (Osterbrock & Ferland 2006), hence, we assumed an electron density of $n_e \sim 100 \text{ cm}^{-3}$ for all apertures in our calculations. To obtain the electron temperature $T_e(\text{OIII})$ we used the five level atomic model FIVEL (De Robertis et al. 1987), implemented under the IRAF STS package NEBULAR. This program has been developed to obtain the physical conditions in a low-density nebula, given appropriate emission line ratios. Figure 8b shows the $[\text{OIII}]\lambda\lambda 4959, 5007/[\text{OIII}]\lambda 4363$ emission line ratio used to calculate the electron temperature $T_e(\text{OIII})$, and Figure 8c shows the resulting spatial distribution of electron

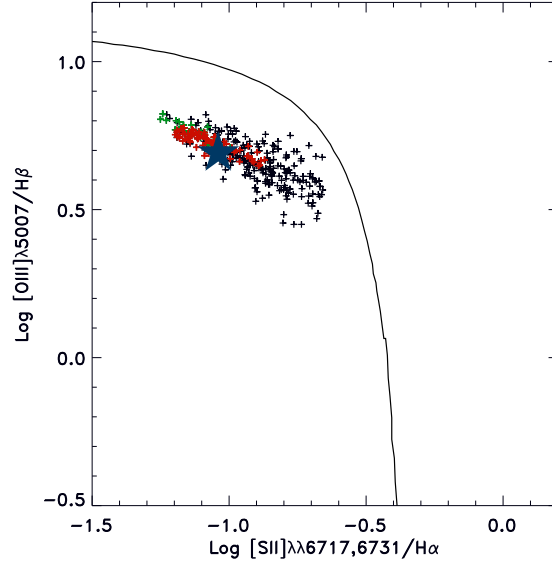


Fig. 7.— [OIII]/H β versus [SII]/H α diagnostic diagram for the original data points presented in Figure 6a) and c). Red crosses correspond to region A, green crosses to region B and the black crosses to the outer part of the galaxy. The integrated value for the galaxy is represented by the blue star. The solid line is the dividing line between HII galaxies and AGNs (Osterbrock & Ferland 2006).

temperature $T_e(\text{OIII})$. The range of valid data points varies from 1.20 to 1.70×10^4 K with a standard deviation of 0.1×10^4 K for the original data set and from ~ 1.37 to $\sim 1.53 \times 10^4$ K with a standard deviation of 0.03×10^4 K for the smoothed data points. The total oxygen abundances for each aperture are obtained assuming the contribution of O^+ and O^{++} ions, thus we have that

$$\frac{O}{H} = \frac{O^+}{H^+} + \frac{O^{++}}{H^+}, \quad (3)$$

where the $T_e(\text{OII})$ temperature and the O^+ and O^{++} ions are obtained assuming the expressions given by Pagel et al. (1992).

Figure 9a shows the spatial distribution of the oxygen abundances over the regions where the emission line [OIII] $\lambda 4363$ was detected. The oxygen abundance values in units of $12 + \log(\text{O}/\text{H})$ range from 7.70 ± 0.08 to 7.84 ± 0.04 with a maximum error of ~ 0.12 dex, an average value of 7.77 and a standard deviation of 0.10 dex. However, the smoothed map has values from ~ 7.69 to ~ 7.86 with a standard deviation of ~ 0.04 dex. Figure 9b shows

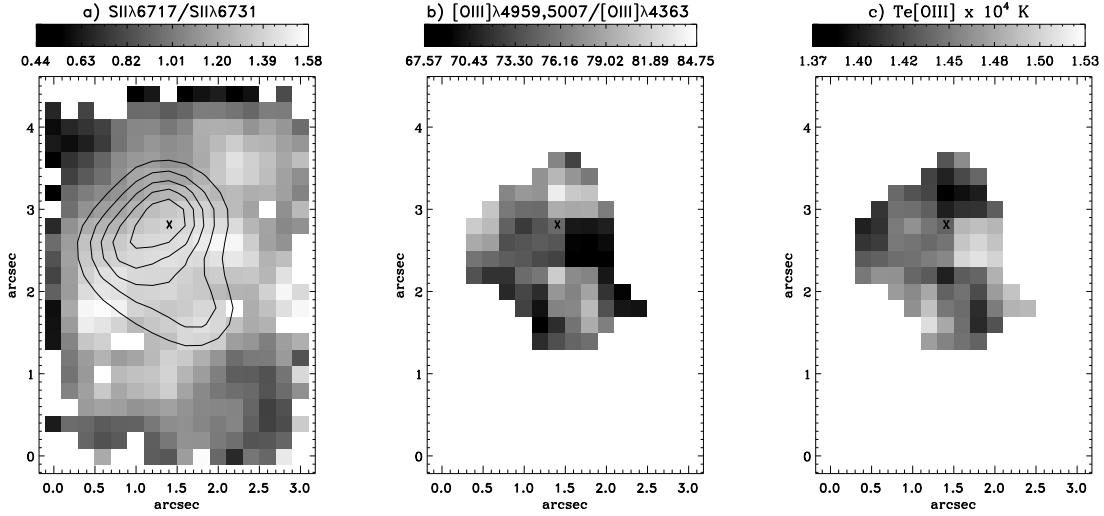


Fig. 8.— (a) $[\text{SII}]\lambda 6717/[\text{SII}]\lambda 6731$ ratio map used to calculate the electron density. (b) $[\text{OIII}]\lambda\lambda 4959,5007/[\text{OIII}]\lambda 4363$ emission line ratio, which is used to calculate the electron temperature $T_e(\text{OIII})$. (c) $T_e(\text{OIII})$ electron temperature in units of 10^4K . The maximum $\text{H}\alpha$ emission is placed over region A and is indicated in the maps by an X symbol. $\text{H}\alpha$ contours are overplotted on the maps.

the radial distribution of oxygen abundance with respect to the $\text{H}\alpha$ peak emission within a region $\lesssim 0.4$ kpc. Statistically the bulk of the original data points are lying in a region of 2σ dispersion ($\sigma=0.1$ dex) around the average value. The 2σ dispersion is represented by the dotted lines. A least fit square with a slope of -0.14 ± 0.06 dex kpc^{-1} was found, using all original data points in Figure 9b. The error in the gradient is obtained directly from the linear regression. In the same Figure we show the radial distribution of the smoothed data points as light blue triangles. These results indicate that there is no significant variations across the galaxy. At most, we can say that there is a very marginal gradient of a decreasing abundance from the center outwards, indicating that, on average, the highest abundance values are found near the peak $\text{H}\alpha$ emission.

3.5. Velocity field

The internal structure of HII galaxies and GHIIRs, as viewed in the ionized gas, is directly associated with mechanisms of photoionization, magnetic field induced turbulence, and feedback by the current episode of massive star formation and evolution, i.e. radiative shocks, stellar and supernovae driven-winds. All of it, under the influence of the gravi-

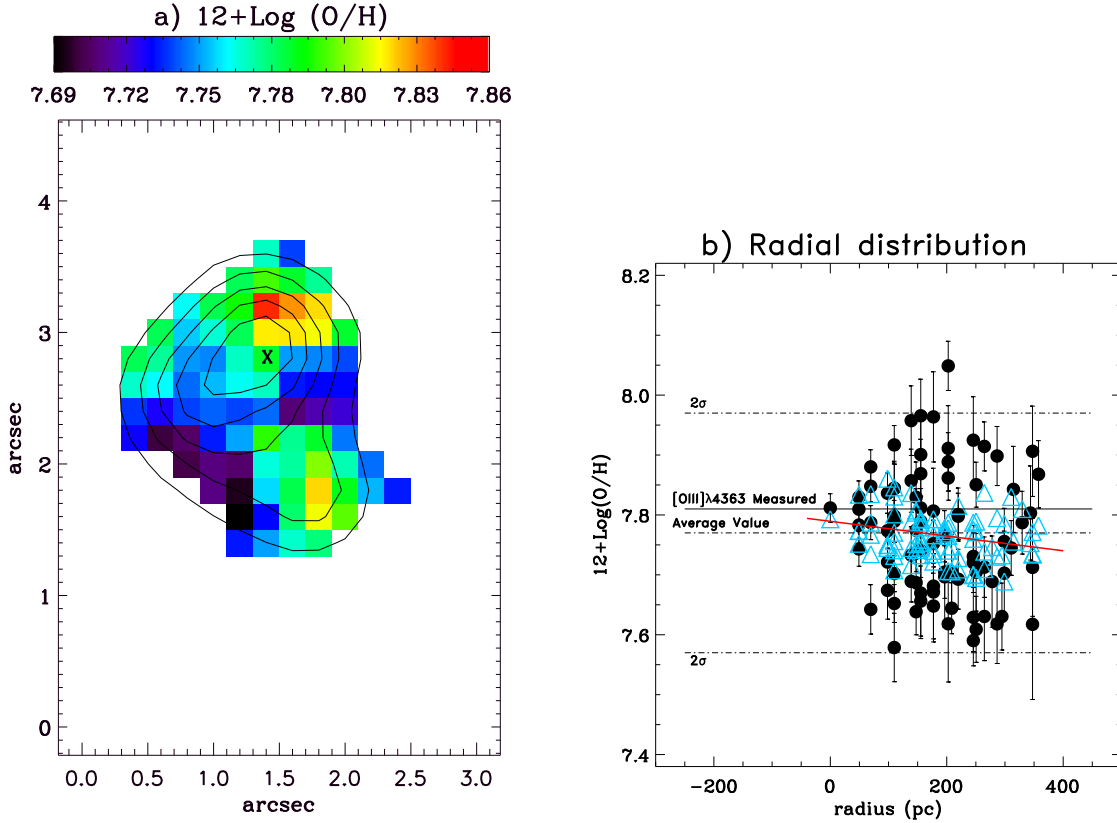


Fig. 9.— Oxygen abundances $[12+\text{Log}(\text{O}/\text{H})]$: (a) Spatial distribution. The isocontours display the $\text{H}\alpha$ emission. The maximum $\text{H}\alpha$ emission is placed over region A and is indicated in the map by an X symbol. $\text{H}\alpha$ contours are overplotted on the maps. (b) Radial distribution. The central dotted line represents the $12+\text{log}(\text{O}/\text{H})$ average value of 7.77, and the solid line the integrated value of $12+\text{log}(\text{O}/\text{H})=7.81$ in the region where the emission lines $[\text{OIII}]\lambda 4363$ were measured. The difference between the maximum and minimum values in the original data set (black dots) is equal to 0.47 dex. Light blue triangles represents the smoothed $12+\text{Log}(\text{O}/\text{H})$ radial distribution. A least square fit using the original data points is indicated by the red line.

tational potential of the complex of gas and stars. The presence of expanding structures (shells, loops and bubbles) is very common in GHIIRs (e.g., the HST image on NGC 604, Tenorio-Tagle et al. 2000; Chu & Kennicutt 1994, for 30 Doradus). These structures have also been observed in the prototypical HII galaxies as II Zw 40 and their resulting nested filaments have been explained by the effects of photoionization and stellar winds in an inhomogeneous ISM (Tenorio-Tagle et al. 2006). UM 408 shows, in the $\text{H}\alpha$ emission line map

(Figure 4) and in the acquisition broad-band image (Figure 1), an outer regular shape with no signs of large-scale disruption or a galactic wind (see Westmoquette et al. 2007b, and references therein for the case of NGC 1569). The monochromatic maps, presented in this study, do not provide clear evidence of expanding structures, shell like features or filaments.

In order to study the impact of the star formation on its internal kinematic properties, we derived the spatial distribution of radial velocity v_r (heliocentric) and velocity dispersion σ (FWHM/2.355) by fitting a single Gaussian to the $H\alpha$ emission line profiles. Figure 10 shows the radial velocity derived from the shifts of the $H\alpha$ line peak, and dispersion velocity maps calculated by using the following relation

$$\sigma^2(H\alpha) = \sigma_{obs}^2 - \sigma_{inst}^2 - \sigma_{th}^2, \quad (4)$$

where σ_{obs} is the observed $H\alpha$ velocity dispersion, σ_{inst} is the instrumental dispersion, and σ_{th} is a correction for thermal broadening ($\sqrt{kT_e/m_H} \approx 9.1 \text{ km s}^{-1}$ for hydrogen at a temperature of $T_e=10^4 \text{ K}$). We have used a value of $33.4 \pm 1.0 \text{ km s}^{-1}$ for the instrumental dispersion by comparing the nominal value (from Table 3.1) with that measured directly from the calibration lamps in the grism R600 near $H\alpha$, and assigning the error as the rms of the average.

The velocity field (Figure 10a) shows an apparent systemic motion where the east part of the galaxy (near knot B) is blueshifted, while the west part (near knot A) is redshifted, with a relative motion of $\sim 10 \text{ km s}^{-1}$. This motion may contribute to broaden the integrated line profile over the extent of the whole galaxy. However, it is not enough to explain the total integrated supersonic line width observed of $\sigma = 18.6 \pm 1.5 \text{ km s}^{-1}$. Figure 10b shows the velocity dispersion (line width) map over the observed field, ranging values from $\sim 10 \text{ km s}^{-1}$ to $\sim 30 \text{ km s}^{-1}$. The velocity dispersion varies little across the field, but some points are worth noting. This map is characterized by a subsonic area near region A, while the highest values are located in the outer part of the field of view near region B. The one pixel line width over knot A (the brightest region) has a low σ of $17.1 \pm 1.0 \text{ km s}^{-1}$. This value is identical to a synthetic aperture of $2.7''$ over knot A. This synthetic aperture was chosen to mimic the single fiber high dispersion observation of Bordalo (2004) who find $\sigma=19.6 \pm 0.4 \text{ km s}^{-1}$, that is consistent with our results.

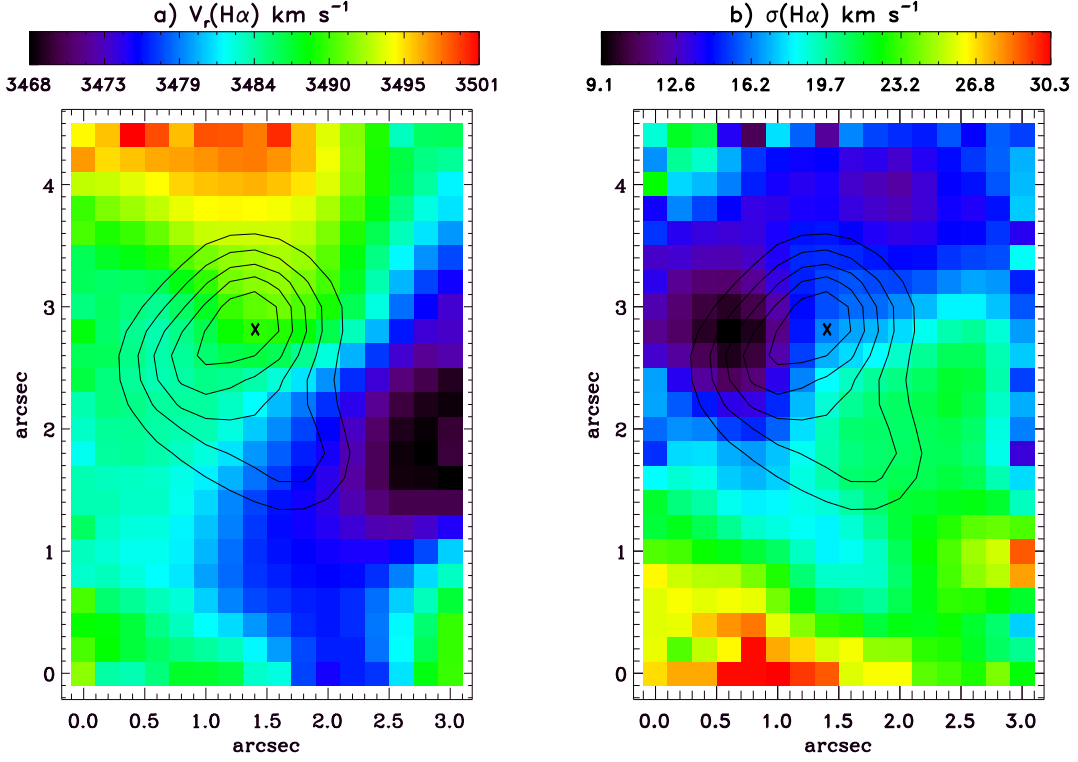


Fig. 10.— (a) $H\alpha$ radial velocity in units of km s^{-1} . (b) $H\alpha$ Velocity dispersion σ . The value showed in this figure is obtained considering an instrumental σ_{inst} and thermal σ_{th} correction over the observed value σ_{obs} . The maximum $H\alpha$ emission is placed over region A and is indicated in the maps by an X symbol.

4. Discussion

4.1. The integrated properties of UM 408

We have measured the flux in two different apertures enclosing more than $\sim 60\%$ of the observed $H\alpha$ flux of the galaxy in order to study the properties of the star formation regions detected in this galaxy. One aperture for region A (48% of the measured $H\alpha$ flux) and another for region B (13% of the measured $H\alpha$ flux). These regions have a diameters of about $1''.5$ and $1''$ that correspond to approximately 375 pc and 250 pc, respectively. Regions A and B are indicated in the $[OIII]\lambda 5007$ map of Figure 4. These regions are formed by the data points where the $[OIII]\lambda 4363$ emission line is detected. To obtain the integrated properties of the galaxy and compare with previous observations (e.g. Masegosa et al. 1994; Pustilnik et al. 2002) we derived the integrated spectra summing over all pixels in our data cube. Table 2

summarizes the resultant emission line values, obtained using the different synthetic apertures, including the total [OIII] λ 4363 aperture over the galaxy (in regions where [OIII] λ 4363 emission line is detected and measured). These measurements are in reasonable agreement with those derived with long slit spectroscopy (e.g., Terlevich et al. 1991; Masegosa et al. 1994; Pustilnik et al. 2002) considering aperture differences and observational uncertainties. A larger discrepancy however occurs between our observed [OII] λ 3726,29/H β value of 0.52 and that of Pustilnik et al. (2002) of 1.45. However, their value must be overestimated since, from their Figure 1, we clearly see that H β > [OII] λ 3727.

The observed EW(H β) values in UM 408 are \sim 102 Å and \sim 57 Å for regions A and B and \sim 67 Å for the integrated galaxy, respectively. The values for regions A and B have been calculated by taking the average over all pixels in each region. Using these EW(H β) values we can estimate the cluster ages by comparison with the values obtained from STARBURST99 model (Leitherer et al. 1999). The resulting ages assuming an instantaneous burst and a metallicity of Z=0.004 for a Salpeter IMF with a mass limit of 1M $_{\odot}$ to 100M $_{\odot}$ are 4.83 Myrs and 5.00 Myrs for regions A and B, respectively. These ages are consistent with both regions being formed simultaneously. We found integrated luminosities (assuming a distance of D=46.8 Mpc; Pustilnik et al. 2002) of Log L(H α)=39.15, 38.58 and 39.47 erg s $^{-1}$ for regions A and B and for the integrated galaxy, respectively. These correspond to a star formation rate of SFR=0.011, 0.003 and 0.024 M $_{\odot}$ yr $^{-1}$, and with a number of ionizing photons log Q(H 0)=51.01, 50.45 and 51.34 photons s $^{-1}$ for regions A, B and for the integrated galaxy, obtained from the relationships given by Kennicutt (1998). The masses of these regions can be estimated by scaling the number of ionizing photons with the models predicted for the corresponding ages. The stellar masses are 5.17×10^4 M $_{\odot}$ and 2.29×10^4 M $_{\odot}$ for regions A and B, respectively. Table 3 shows the derived integrated properties of the galaxy and its star forming regions.

Since its discovery, UM 408 was classified as a low abundance galaxy with an integrated value of 12+Log(O/H)=7.63 for low resolution spectroscopy (Masegosa et al. 1994) and 7.93 for high resolution spectroscopy (Pustilnik et al. 2002). In this work, we found an integrated abundance (summing over all spaxels in our field of view) of 12+Log(O/H)=7.87 \pm 0.05. The synthetic apertures previously mentioned, yield an integrated oxygen abundance of 12+Log(O/H)=7.82 \pm 0.05 and 7.84 \pm 0.06 for regions A and B, respectively. Measuring the abundance in an aperture equivalent with the area where the emission line [OIII] λ 4363 was measured we obtain a value of 7.81 \pm 0.05, the same value obtained in the peak of the H α emission (see Figure 9b). This result reflects the fact that the integrated values are light weighted and dominated by the galaxy peak emission.

Finally, despite the fact that a detailed kinematic analysis is beyond the scope of the

present paper, our results confirm that the core dominates the kinematic information of the star forming region, and present a low σ value, as found by other works (e.g., Telles et al. 2001, and references therein). Therefore, a single Gaussian fit to the line profile of any aperture encompassing the brightest knot will measure a representative line width of the dominant supersonic motions, somewhat deconvolved by the effects of stellar and SN mechanical energy input. The effects of stellar or SN feedback will contribute to the broadening of the line profiles, but will only be detectable in the lower density regions at low intensities. One means to recognize these effects is through the identification of inclined bands in the diagnostic diagrams of intensity vs. σ as proposed by Muñoz-Tuñón et al. (1996) and Yang et al. (1996). However, the compactness of UM 408 and the small range of reliable line widths make the use of the diagnostic diagrams difficult to interpret in this case. The H α line profile is symmetric and well represented by a single Gaussian, and does not show prominent low intensity wings in either apertures. An attempt to deblend a possible additional component to this line profile produced only an upper limit of $\sigma_{broad} \leq 100 \text{ km s}^{-1}$ with $F(\alpha)_{broad}/F(\alpha)_{narrow} \leq 3\%$.

4.2. Distribution of the oxygen abundance and their comparison with other dwarf galaxies

The uniform behavior of O/H abundance in scales of hundreds of pc in low mass galaxies as in UM 408 is not without precedent, and is comparable with the observed variation in some dwarf galaxies by other authors. In NGC 4214 (Dwarf Irregular/Wolf-Rayet galaxy) Kobulnicky & Skillman (1996) showed that there is no localized O, N or He abundance gradients, but they found, near the youngest region, an oxygen overabundance of 0.095 ± 0.019 dex. Kobulnicky & Skillman (1997), using long slit spectroscopy to study the interstellar medium of the dwarf irregular galaxy NGC 1569, failed to find evidence for O/H gradient from the recent star formation activity. Lee et al. (2006) studied the local group dwarf irregular galaxy NGC 6822 and measured a difference of $\Delta(\text{O}/\text{H}) = 0.53$ dex between the maximum (8.43 ± 0.2) and minimum value (7.90 ± 0.1), with a mean oxygen abundance of $12 + \log(\text{O}/\text{H}) = 8.11 \pm 0.1$ using only the HII regions where the [OIII] $\lambda 4363$ emission lines were detected. A gradient of -0.14 ± 0.07 dex kpc^{-1} was measured by Lee et al. in a radius $\lesssim 1.4$ kpc, and a slope of -0.16 dex kpc^{-1} was obtained if measurements from the literature were included, showing the existence of a possible radial gradient in oxygen abundance. Izotov et al. (2006) using VLT/GIRAFFE in the ARGUS mode, observed the dwarf galaxy SBS 0335-052E, one of the most metal poor galaxies with an integrated oxygen abundance of $12 + \log(\text{O}/\text{H}) = 7.30$ (Melnick et al. 1992). The spatial distribution of the oxygen abundance in the ISM of SBS 0335-052E vary from 7.00 ± 0.08 to 7.42 ± 0.02 , representing a difference

of $\Delta(\text{O}/\text{H})=0.42$ dex. The maximum value of oxygen abundances in this galaxy does not correspond to the position of one of the identified SSCs, but Izotov et al. find a slight trend of a decreasing abundance, interpreted as possible self-enrichment. However, they argue that the errors in the calculated oxygen abundances and T_e , n_e , etc, not considering instrumental and observational uncertainties, lead to consider the oxygen abundance variations in SBS 0335-052E may not be statistically significant. More recently, using IFU-PMAS observations, Kehrig et al. (2008) studied the spatial distribution of some metals over the galaxy IIZw70. In this study they find a difference of $\Delta(\text{O}/\text{H})=0.40$ dex between the maximum (8.05 ± 0.06) and minimum (7.65 ± 0.06) values of oxygen abundance. In the case of UM 408, the bulk of our observed data points are distributed in a region of $\pm 2\sigma$ dispersion around the average value with a difference between the maximum and minimum values of 0.47 dex. This is, somewhat, in good agreement with previous results in other dwarf galaxies, using in some cases different techniques. We note that the gradient found in our work, calculated in a spatial scale of hundreds of pc, is similar to the gradients calculated in other studies in scales of kpc. Finally, the two giant regions A and B show a difference of oxygen abundance of only $\Delta(\text{O}/\text{H})=0.02$ dex, which indicates that these regions show identical chemical properties within the errors. Given the ages (~ 5 Myr) and stellar masses ($\sim 10^4 M_\odot$) of these regions, we expect that hundreds of SNs have exploded, producing eventually localized enrichments. But the absence of chemical overabundances in the ISM of UM 408 and in the dwarf galaxies studied in the literature lead to conclude that the population of young clusters have not produce preferentially localized overabundances.

These results are compatible with the interpretation that the newly synthesized metals from the current star formation episode may not be in the warm phase of the ISM, and thus are not observed at optical wavelengths. The metals that are observed, however, ought to be from previous events, and may be well mixed and homogeneously distributed over the whole extent of this low mass and compact galaxy. Note that in UM 408, there is no bar induced rotation, or shear, to produce the metal dispersal and mixing as in more massive galaxies (e.g., Roy & Kunth 1995), and thus there must be another mechanism responsible for the large-scale dispersal and mixing with the ISM. One such hydrodynamic mechanism for the transport and mixing of the metals produced by compact bursts of star formation into the ISM has been proposed by Tenorio-Tagle (1996). This model predicts that the energy injected by core-collapse supernovae change the physical conditions (density and temperature) of the interstellar medium, while undergoing a long excursion into the galactic volume. The injected matter is first thermalized, near the starburst, as it goes through a reverse shock. This generates the giant pressure that allows for the built up of superbubbles, kpc scale structures that may grow for up to 50 Myr. Afterwards, once the SN II phase is over, the giant superbubble gas begins to cool down by radiation. This happens first within

the parcels of gas that present the largest densities, promoting their thermal instability. The sudden loss of pressure within densest parcels of gas would immediately trigger the appearance of re-pressurizing shocks emanating from the low density hot gas. The process leads to a plethora of dense condensations that inevitably will fall and settle within the main body of the galaxy. The process of cooling and dispersal onto the main body of the galaxy will occur within a few 10^8 yr. For a complete mixing, the model assumes that a further star formation episode has to occur and through photoionization the metal enrich condensations will expand and be fully mixed with the ISM (see also Stasinska et al. 2007). This scenario seems plausible and compatible with our analysis for the case of UM 408.

5. Conclusions

We used GMOS-IFU spectrum of the compact HII galaxy UM 408, in order to derive the spatial distribution of emission line ratios, extinction $c(\text{H}\beta)$, radial velocity v_r , velocity dispersion σ , electron temperature and oxygen abundance (O/H) as well the integrated properties over an extended region of $3'' \times 4''.4$ equivalent to 750×1100 pc in the central part of the galaxy. Below, we summarize our results and conclusions.

1. The observed region of the galaxy includes two giant HII regions not resolved in previous studies, here labelled A and B. The sizes of these ionized regions are ~ 375 and ~ 250 pc for regions A and B, respectively. Another region labelled C was found to the East of region B. We do not observe large scale structures as in other GHIIRs and HII galaxies in the monochromatic maps.
2. The distribution of dust content in the galaxy was derived from the Balmer line decrement ($\text{H}\alpha/\text{H}\beta$). The $c(\text{H}\beta)$ distribution concentrates the highest values close but not coincident with the peak of $\text{H}\alpha$ emission in each ionized cluster (A and B). The dust seems to be displaced from the star formation regions by the action of the star cluster winds.
3. We used $[\text{OIII}]/\text{H}\beta$ and $[\text{SII}]/\text{H}\alpha$ ratios to investigate the possible excitation mechanism over the ISM of the galaxy. Comparing the data points in the diagnostic diagram with the theoretical model given by Osterbrock & Ferland (2006), we found that all measured $\text{H}\alpha$ flux arises from gas photoionized by massive stars
4. The velocity field (v_r) shows an apparent systemic motion where the east part of the galaxy (near knot B) is blueshifted, while the west part (near knot A) is redshifted, with a relative motion of $\sim 10 \text{ km s}^{-1}$ and a difference between the maximum and minimum

values of $\sim 33 \text{ km s}^{-1}$. The velocity dispersion map shows supersonic values, typical for extragalactic HII regions, ranging values from $\sim 10 \text{ km s}^{-1}$ to $\sim 30 \text{ km s}^{-1}$.

5. The ages of the two giant regions detected in this study, were estimated from their $\text{EW}(\text{H}\beta)$ and the STARBURST99 models, suggesting that they are coeval events of $\sim 5 \text{ Myr}$ with stellar masses of $\sim 10^4 M_{\odot}$. We see a marginal difference in the integrated oxygen abundance between these regions of $\Delta(\text{O}/\text{H})=0.02 \text{ dex}$.
6. Finally, as found in other nearby dwarf galaxies, we do not observe a gradient in oxygen abundance across the compact galaxy UM 408. The bulk of the observed data points are lying in a region of $\pm 2\sigma$ dispersion ($\sigma=0.1 \text{ dex}$); therefore, the new metals formed in the current star formation episodes are not observed and reside probably in the hot gas phase ($T\sim 10^7 \text{ K}$), whereas the metals from previous star formation events are well mixed and homogeneously distributed through the whole extent of the galaxy.

All results presented here are suggestive that UM 408 is an unevolved low metallicity dwarf galaxy, undergoing a simultaneous episode of star formation over the whole optically observed extension, and it is a genuine example of the simplest starbursts occurring in galactic scale, possibly mimicking the properties one expects for young galaxies at high redshift.

6. Acknowledgments

We would like to thank the anonymous referee for his/her comments and suggestions which substantially improved the paper. PL acknowledges support from Faperj, Brazil for his studentship and IAC Spain where part of this work was done. This work has been partly funded by ESTALLIDOS (see <http://www.iac.es/project/GEFE/estallidos>) project AYA2007-67965-C03-01. ET acknowledges his US Gemini Fellowship by AURA, and GTT acknowledges a research grant 60333 from CONACYT Mexico. Based on observations obtained at the Gemini Observatory, which is operated by the Association of Universities for Research in Astronomy, Inc., under a cooperative agreement with the NSF on behalf of the Gemini partnership: the National Science Foundation (United States), the Science and Technology Facilities Council (United Kingdom), the National Research Council (Canada), CONICYT (Chile), the Australian Research Council (Australia), Ministério da Ciência e Tecnologia (Brazil) and Ministerio de Ciencia, Tecnología e Innovación Productiva (Argentina); Gemini program ID: GS-2004B-Q-59. This research has made use of the NASA/IPAC Extragalactic Database (NED) which is operated by the Jet Propulsion laboratory, California

Institute of technology, under contract with the National Aeronautics and Space Administration.

REFERENCES

- Allington-Smith, J., Graham, M., Content, R., Dodsworth, G., Davies, R., Miller, B. W., Jørgensen, I., Hook, I., Crampton, D., & Murowinski, R. 2002, *PASP*, 114, 892
- Arp, H., & Sandage, A. 1985, *AJ*, 90, 1163
- Arribas, S., Mediavilla, E., Garcia-Lorenzo, B., del Burgo, C., & Fuensalida, J. J. 1999, *A&AS*, 136, 189
- Baldwin J.A., Phillips M.M., & Terlevich R. 1981, *PASP*, 93, 5
- Bordalo Vinicius 2004, Tese de Mestrado Observatório Nacional, Brazil
- Cairós, L. M., Caon, N., García-Lorenzo, B., Vílchez, J. M., & Muñoz-Tuñón, C. 2002, *ApJ*, 577, 164
- Cairós, L. M., Caon, N., Papaderos, P., Noeske, K., Vílchez, J. M., Lorenzo, B. G., & Muñoz-Tuñón, C. 2003, *ApJ*, 593, 312
- Castellanos, M., Díaz, A. I., & Terlevich, E. 2002, *MNRAS*, 329, 315
- Chu, Y., & Kennicutt, R. C., Jr. 1994, *ApJ*, 425, 720
- Conti, P. S., & Vacca, W. D. 1994, *ApJ*, 423, 97
- De Robertis, M. M., Dufour, R. J., & Hunt, R. W. 1987, *JRASC*, 81, 195
- González D., R. M., & Pérez, E. 2000 *MNRAS*, 317, 64
- Hook, I., Jørgensen, I., Allington-Smith, J. R., Davies, R. L., Metcalfe, N., Murowinski, R. G., & Crampton, D. 2004, *PASP*, 116, 425
- Howarth, I. D. 1983, *MNRAS*, 203, 301
- Izotov, Y. I., Schaerer, D., Blecha, A., Royer, F., & Guseva, N. G., North, P 2006, *A&A*, 459, 71
- Kennicutt, R. C. 1998, *ApJ*, 498, 541

- Kehrig, C., Vilchez, J. M., Sánchez, S. F., Telles, E., Pérez-Montero, E., & Martín-Gordón, D. 2008, *A&A*, 477, 813
- Kehrig, C., Telles, E., & Cuisinier, F. 2004, *ApJ*, 128, 1141
- Kobulnicky, H. A., Skillman, E. D., Roy, J. R., Walsh, J. R., & Rosa, M. R. 1997, *ApJ*, 477, 679
- Kobulnicky, H. A., & Skillman, E. D. 1997, *ApJ*, 489, 636
- Kobulnicky, H. A., & Skillman, E. D. 1996, *ApJ*, 471, 211
- Kunth, D., Maurogordato, S., & Vigroux, L. 1988, *A&A*, 204, 10
- Lagos P., Telles E., & Melnick J., 2007, *ApJ*, 476, 89
- Lee, H., Skillman, E. D., & Venn, K. A. 2006, *ApJ*, 642, 813
- Leitherer, C., Schaerer, D., Goldader, J. D., Delgado, R. M. G., Robert, C., Kune, D. F., de Mello, D. F., Devost, D., & Heckman, T. M. 1999, *ApJS*, 123, 3
- Loose, H.-H., & Thuan, T. X. 1986, in *Star Forming Dwarf Galaxies and Related Objects*, ed. D. Kunth, T. X. Thuan, & J. T. T. Van (Gif-sur-Yvette: Editions Frontières), 73
- Masegosa, J., Moles, M., & Campos-Aguilar, A. 1994, *ApJ*, 420, 576
- Maiz-Apellaniz, J., Mas-Hesse, J. M., Muñoz-Tuñón, C., Vilchez, J. M., & Castaneda, H. O. 1998, *A&A*, 329, 409
- Melnick J., Moles M., Terlevich R., & Garcia-Pelayo J.M., 1987, *MNRAS*, 226, 849
- Melnick J., Terlevich R., & Moles M. 1988, *MNRAS*, 235, 297
- Melnick, J., Heydari-Malayeri, M., & Leisy, P. 1992, *A&A*, 253, 16
- Muñoz-Tuñón, C., Tenorio-Tagle, G., Castañeda, H. O., & Terlevich, R. 1996, *AJ*, 112, 1636
- O'Connell, R. W., Gallagher, J. S., & Hunter, D. A. 1994, *ApJ*, 433, 65
- Osterbrock, D. E., & Ferland, G. J. 2006 *Astrophysics of Gaseous Nebulae and Active Galactic nuclei*, 2nd. edn.
- Pagel, B. E. J., Simonson, E. A., Terlevich, R. J., & Edmunds, M. G. 1992, *MNRAS*, 255, 325

- Papaderos, P., Loose, H.H., Thuan, T. X., & Fricke, K. J. 1996, *A&AS*, 120, 207
- Pustilnik, S. A., Kniazev, A. Y., Masegosa, J., Márquez, I. M., Pramskij, A. G., & Ugryumov, A. V. 2002, *A&A*, 389, 779
- Roy, J.-R., & Kunth, D. 1995, *A&A*, 294, 432
- Salzer, J. J. 1989, *ApJ*, 347, 152
- Salzer, J. J., Rosenberg, J. L., Weisstein, E. W., Mazzarella, J. M., & Bothun, G. D. 2002, *ApJ*, 124, 191
- Sargent, W. L. W., & Filippenko, A. V. 1991, *ApJ*, 102, 107
- Seaton, M. J. 1979, *MNRAS*, 187, 73
- Stasinska, G, Tenorio-Tagle, G, Rodriguez, M., & Henney, W. 2007, *A&A*, 471, 193
- Telles, E. 1995, Ph.D. thesis, University of Cambridge
- Telles, E., & Terlevich, R. 1997, *MNRAS*, 286, 183
- Telles, E., Melnick, J., & Terlevich, R. 1997, *MNRAS*, 288, 78
- Telles, E., Muñoz-Tuñón, C., & Tenorio-Tagle, G. 2001, *ApJ*, 548, 671
- Tenorio-Tagle, G., Muñoz-Tuñón, C., Pérez, E., Silich, S., & Telles, E. 2006, *ApJ*, 643, 186
- Tenorio-Tagle, G., Muñoz-Tuñón, C., Pérez, E., Maíz-Apellániz, J., & Medina-Tanco, G. 2000, *ApJ*, 541, 720
- Tenorio-Tagle, G. 1996, *ApJ*, 111, 1641
- Tenorio-Tagle G., Muñoz-Tuñón C., & Cox D. P. 1993, *ApJ*, 418, 767
- Terlevich R., & Melnick J. 1981, *MNRAS*, 195, 839
- Terlevich R., Melnick J., Masegosa J., Moles M., & Copetti M.V.F. 1991, *A&AS*, 91, 285
- Walsh, J. R., & Roy, J. R. 1989, *MNRAS*, 239, 297
- Westera, P., Cuisinier, F., Telles, E., & Kehrig, C. 2004, *A&A*, 423, 133
- Westmoquette, M. S., Exter, K. M., Smith, L. J., & Gallagher, J. S. 2007a, *MNRAS*, 381, 894

Westmoquette, M. S., Smith, L. J., Gallagher, J. S., & Exter, K. M. 2007b, MNRAS, 381, 913

Whitmore, B., & Schweizer, F. 1995, AJ, 109, 960

Whitmore, B. C., Zhang, Q., Leitherer, C., Fall, S. M., Schweizer, F., Miller, & B. W. 1999, AJ, 118, 1551

Yang, H., Chu, Y. H., Skillman, E. D., & Terlevich, R. 1996, ApJ, 112, 146

Table 1. Observational setup

Grating	Central Wavelength (\AA)	Airmass	Exposure Time (seconds)	Resolution (\AA)	Dispersion ($\text{\AA}/\text{pixel}$)	Seeing ($''$)
(1)	(2)	(3)	(4)	(5)	(6)	(7)
B600	4300	1.24	1 \times 1800	1.98	0.45	0.8
R600	5850	1.47	2 \times 2000	1.67	0.47	0.9

Table 2. Observed emission line fluxes for the integrated galaxy and regions A and B .
Fluxes normalized to $F(\text{H}\beta)$.

	Integrated galaxy (1)	[OIII] λ 4363 measured (2)	Region A (3)	Region B (4)
[SII] λ 6731	0.24 \pm 0.01	0.20 \pm 0.03	0.20 \pm 0.03	0.20 \pm 0.04
[SII] λ 6717	0.32 \pm 0.01	0.28 \pm 0.04	0.27 \pm 0.03	0.27 \pm 0.04
[NII] λ 6584	0.13 \pm 0.01	0.11 \pm 0.03	0.11 \pm 0.02	0.10 \pm 0.03
H α	5.94 \pm 0.07	6.07 \pm 0.29	6.14 \pm 0.28	5.87 \pm 0.28
[OIII] λ 5007	5.24 \pm 0.21	5.33 \pm 0.30	5.30 \pm 0.25	5.60 \pm 0.36
[OIII] λ 4959	1.71 \pm 0.18	1.72 \pm 0.11	1.71 \pm 0.11	1.80 \pm 0.11
[OIII] λ 4363	0.06 \pm 0.01	0.07 \pm 0.01	0.07 \pm 0.01	0.07 \pm 0.02
H γ	0.29 \pm 0.01	0.31 \pm 0.04	0.31 \pm 0.04	0.36 \pm 0.05
[OII] $\lambda\lambda$ 3726,29	0.52 \pm 0.17	0.30 \pm 0.05	0.32 \pm 0.04	0.27 \pm 0.05
F(H β)	39.70 \pm 0.20	24.93 \pm 0.86	18.63 \pm 0.62	5.09 \pm 0.17

Note. — Fluxes normalized to $F(\text{H}\beta)$ in units of $\times 10^{-16}$ erg s $^{-1}$ cm $^{-2}$. Column (1): Integrated galaxy correspond with the values obtained from the sum of all spaxels in the data cube. Column (2): [OIII] λ 4363 measured correspond with sum of all apertures in the maps where [OIII] λ 4363 was measured. Columns (3) and (4): Regions defined in Figure 4.

Table 3. Integrated properties of the observed area of UM 408.

	Integrated galaxy (1)	[OIII] λ 4363 measured (2)	Region A (3)	Region B (4)
$c(\text{H}\beta)$	0.93 \pm 0.02	0.96 \pm 0.06	0.97 \pm 0.06	0.91 \pm 0.06
Te(OIII) $\times 10^4$ (K)	1.40 \pm 0.08	1.45 \pm 0.14	1.45 \pm 0.12	1.44 \pm 0.16
Te(OII) $\times 10^4$ (K)	1.32 \pm 0.11	1.34 \pm 0.18	1.34 \pm 0.16	1.34 \pm 0.21
n_e (cm $^{-3}$)	\sim 100	\sim 100	\sim 100	\sim 100
$\log[\text{OIII}]\lambda 5007/\text{H}\beta$	0.69 \pm 0.02	0.70 \pm 0.02	0.69 \pm 0.02	0.72 \pm 0.03
$[\text{SII}]/\text{H}\alpha$	0.09 \pm 0.01	0.08 \pm 0.01	0.07 \pm 0.01	0.08 \pm 0.02
$\text{O}^+/\text{H}^+ \times 10^5$	1.16 \pm 0.26	0.64 \pm 0.09	0.70 \pm 0.09	0.57 \pm 0.10
$\text{O}^{++}/\text{H}^+ \times 10^5$	6.35 \pm 0.58	5.88 \pm 0.68	5.85 \pm 0.60	6.31 \pm 0.82
$12+\log(\text{O}/\text{H})$	7.87 \pm 0.05	7.81 \pm 0.05	7.82 \pm 0.05	7.84 \pm 0.06
$\log L(\text{H}\alpha)$ (erg s $^{-1}$)	39.47	39.27	39.15	38.58
\log (number of photons) (photons s $^{-1}$) †	51.34	51.14	51.01	50.45
SFR(M_\odot yr $^{-1}$) †	0.024	0.015	0.011	0.003
EW(H β) (\AA)	62	89	102	57
Age (Myr) ††	...	4.73	4.83	5.00

Note. — † Number of photons and SFR were obtained using the relations given by Kennicutt (1998). †† Ages were obtained using the STARBURST99 predictions model, assuming an instantaneous star formation and a Salpeter IMF from 1 to 100 M_\odot .